nature nanotechnology

Supplementary information https://doi.org/10.1038/s41565-024-01728-9

Electrically tunable space–time metasurfaces at optical frequencies

In the format provided by the authors and unedited

Table of Contents

S1: Realizing active metasurfaces at optical frequencies

Space-time metasurfaces operating at microwave frequencies have been previously demonstrated. While the conceptual framework for space-time modulation is common to both microwave and optical frequency domains, fundamentally different challenges must be overcome to achieve active metasurfaces in the optical domain.

For example, a common method of modulating a single metasurface element in the microwave regime is switching a positive-intrinsic-negative (PIN) diode (~ mm scale) connected to metallic patches between its low resistance "ON" state (forward bias) and high resistance "OFF" state (negative bias) which changes the amplitude and phase of the electromagnetic (EM) field scattered from that element [1,2]. This technique is very effective at achieving a large modulation at microwave frequencies because the carrier injection is efficient and can be modeled using the Drude model where the change in permittivity will be proportional to $\Delta N/\omega$, where ΔN is the change in carrier concentration and ω is the angular frequency of incident radiation [3]. Thus, at microwave frequencies, a small change in carrier concentration will result in a large change in permittivity, providing significant amplitude and phase modulation.

By contrast, in the optical domain, the higher frequency gives rise to substantially smaller changes in permittivity, so that any material change from carrier accumulation (as in our devices) will result in a very small change in amplitude and phase of scattered light. As a result, active metasurfaces must be coupled to geometric resonances to enhance the light-matter interactions and to obtain significant optical modulation. This is an ongoing challenge in materials selection, device design and metasurface fabrication. It should also be noted that our approach for electrically tuning phase and amplitude of active optical metasurfaces inherently allows for continuous tunability. By contrast, a single PIN diode can only achieve two different states of phase and amplitude, and multiple diodes must be added to a unit cell to obtain more than two phase or amplitude steps [4]. As a result, our active optical metasurfaces can steer to arbitrary angles with high directivity by exploiting continuous phase tuning without requiring redesign of our subwavelength structures [5].

Another difference is in the nature of electrical interconnects. In the microwave regime, where the wavelength is of order ~10s of mm, individual scatterers can be easily addressed with electrical interconnects that are deeply subwavelength, which does not affect the scattering performance. In the optical domain, the design approach must be fundamentally different because electrical interconnects even with dimensions < 1 μm can significantly affect scattering and wavefront control.

In summary, we note there are distinct challenges in the design and realization of active space-time metasurfaces at optical frequencies as compared to those at microwave frequencies. We address these challenges for electrically modulated space-time metasurfaces at optical frequencies for the first time.

S2: Frequency domain/far-field calculations

To calculate the spatiotemporal response of our metasurface, we make use of a two-dimensional Fourier transform of the electric field scattered from our metasurface in space and time. As illustrated in Fig. 1a of the main text, a spatial Fourier transform of the field across our metasurface provides the far-field intensity in space (top plots) and a temporal Fourier transform provides the reflected frequency spectrum (middle plots). By combining these two transforms, we can predict the expected intensity reflected from our metasurface as a function of frequency and angle.

For all calculated intensity plots as a function of frequency and angle in the main text, we first start by discretizing the selected driving voltage signal. Figure S1a shows an example driving waveform which was used to generate the single 1 MHz signal in the main text. Next, using Fig. 2f from the main text, we calculate the expected reflectance/amplitude from the metasurface as a function of time (Fig. S1b). Note: throughout this work, we define reflectance as the magnitude squared of amplitude. At this point, the magnitude squared of the Fourier transform of the time-varying amplitude in Fig. S1b would provide the expected frequency-dependent intensity of reflected light. This frequency spectrum is plotted in Fig. S1c. Note that this spectrum includes negative frequencies as well as the 0^{th} harmonic. As expected, the signal in the 1^{st} harmonic is multiple orders of magnitude than the higher harmonics (consistent with our measurements) but it is many orders of magnitude smaller than the unmodulated 0^{th} harmonic which is not directly measured in our experiments. See Supplementary Section 4 for a detailed description of the total power sent to the 0^{th} harmonic.

To calculate the full space-time response of our metasurface, we first find the time-varying amplitude for the second antenna group by again using the reflectance/voltage relationship in Fig. 2f of the main text and the time-varying voltage signal sent to these antennas. Figure S1d plots the scattered amplitude of the time-varying field for both antenna groups when modulating in the out-of-phase condition shown in Fig. 4b of the main text. We can use the two time-varying field profiles from Fig. S1d to create a matrix of the scattered field in space and time (Fig. S1e). Finally, we take a two-dimensional Fourier transform of this matrix and plot the magnitude squared of the output field in Fig. S1f to obtain the expected intensity as a function of frequency and angle. Again, as expected, we see diffraction at the +/- 1^{st} harmonics while the strongest signal appears at the 0^{th} harmonic. Since we do not detect the unmodulated signal in experiment, all plots in the main text are cut off shortly above 0 MHz. Additionally, it should be noted that the Fourier transforms shown in Fig. S1 and the main text include many more temporal periods than are shown below and use padded zeros to improve resolution.

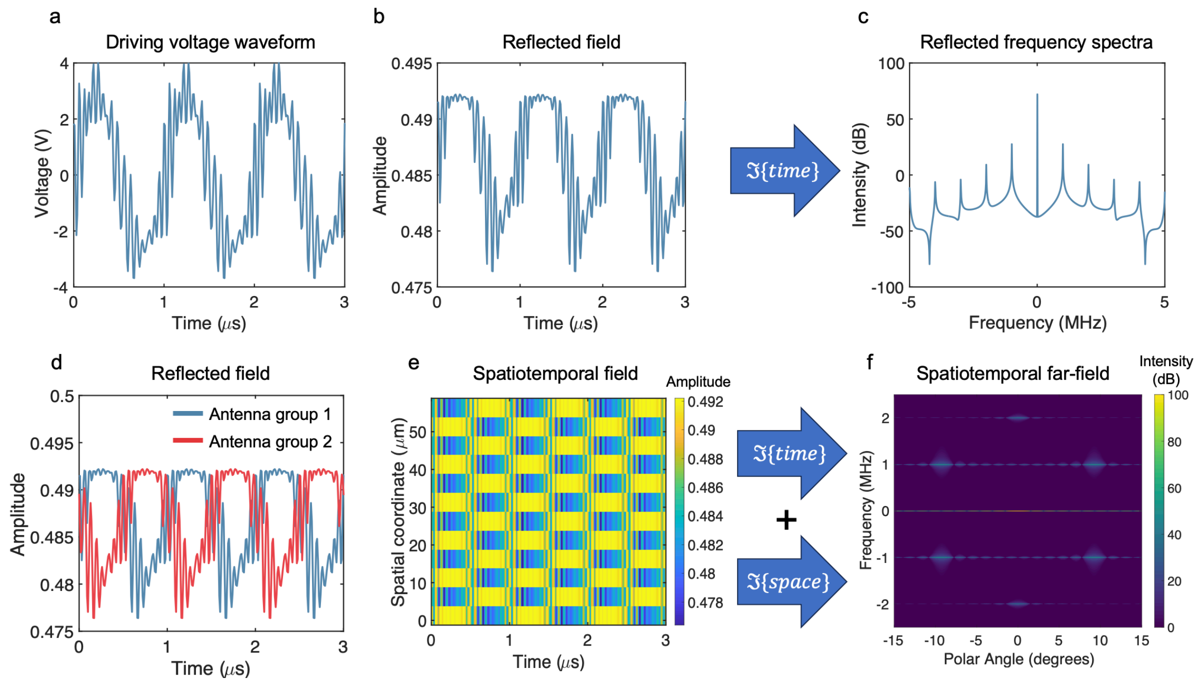

<u>Figure S1:</u> Calculation of far-field intensity. (a) Optimized time-varying voltage signal. (b) Amplitude of field reflected from metasurface when all antennas are driven with voltage signal in (a). (c) Magnitude squared of Fourier transform of signal shown in (b) providing reflected frequency spectrum. (d) Amplitude of field reflected from each metasurface antenna group when driving metasurface in out-of-phase condition from Fig. 4b of main text. (e) Spatiotemporal scattered field across 6 metasurface periods in space and 3 periods in time for out-of-phase condition in Fig. 4b of main text. (f) Magnitude squared of two-dimensional Fourier transform of (e) providing far-field reflected intensity from metasurface as a function of frequency and angle.

S3: Total efficiency of space-time diffraction

At the operating wavelength in this work (λ = 1530 nm), our devices have a reflectance of ~ 24% at 0 V bias. However, at this wavelength, the amplitude and phase modulation depth are relatively small and thus the overall diffraction efficiency will be limited. During 'quasi-static' (purely spatial) diffraction, this means that a significant amount of power will be sent to the 0^{th} spatial order instead of the diffraction orders. Analogously, in purely time-modulation, the majority of light will be unmodulated and remain in the 0^{th} harmonic. However, for the space-time measurements in this work, we use a photodiode and spectrum analyzer to capture only the modulated frequencies reflected from our metasurface and, thus, we do not detect the strong 0^{th} harmonic signal. Because of this capability, we are able to study our space-time metasurfaces with excellent signal-to-noise ratio (SNR) without being limited by modulation depth. In this section, we account for the strong 0^{th} harmonic signal to analyze the total diffraction efficiency achieved during space-time modulated diffraction.

Figure S3a shows a Fourier plane camera image of the light reflected from our metasurface during space-time modulation. The metasurface modulation setup is identical to the situation portrayed in Fig. 4b in the main text. Because our camera captures all frequencies at once (including the unmodulated 0^{th} harmonic), we see that the image is dominated by light at the 0^{th} spatial order, which corresponds to the 0^{th} harmonic light. From this image, it is impossible to distinguish the diffracted orders from the 0^{th} order. Figure S3b shows the light reflected from our metasurface when all elements are held at an identical, constant voltage. The pixel-by-pixel subtraction of Fig. S3b from Fig. S3a is plotted in Fig. S3c and re-normalized in Fig. S3d for ease of visualization. We can now clearly see the diffraction orders created by our space-time modulation, indicated by the red circles. Figure S3e shows an unsaturated image of light reflected from the unmodulated metasurface. (This is Fig. S3b with a 1000x shorter exposure time.) In order to find the total diffraction efficiency from our space-time metasurface, we used the following definition:

$$\eta = \frac{P_{-1} + P_{+1}}{P_{-1} + P_{+1} + P_0} \times \bar{R} \tag{1}$$

where η is diffraction efficiency, $P_{-1,0,+1}$ refer to the power (integrated intensity) in the -1^{st}, 0^{th} and +1^{st} diffraction orders, respectively, and $\bar{R}$ is the average total reflectance. This was calculated by summing the pixel counts in the two diffracted orders in Fig. S3c, dividing by the pixel count in the 0^{th} order of Fig. S3e, dividing by 1000 (to account for the difference in exposure time), then multiplying by the average reflectance across the metasurface ~ 23.5%. This calculation provides a total diffraction efficiency of ~ 0.0036%.

By performing a similar calculation on the data plotted in Fig. S1f, we can compare this experimentally approximated efficiency to the expected efficiency of diffraction. (Note: in this case, we summed the intensity from diffraction in the +/- 1^{st} diffraction orders for both the +1 MHz and -1 MHz signals.) This calculation provides a total efficiency of ~ 0.0017%, which is only roughly a factor of two different from our measured value. This agreement between measurement and calculation provides further validation to our experimental setup, device characterization, and modeling.

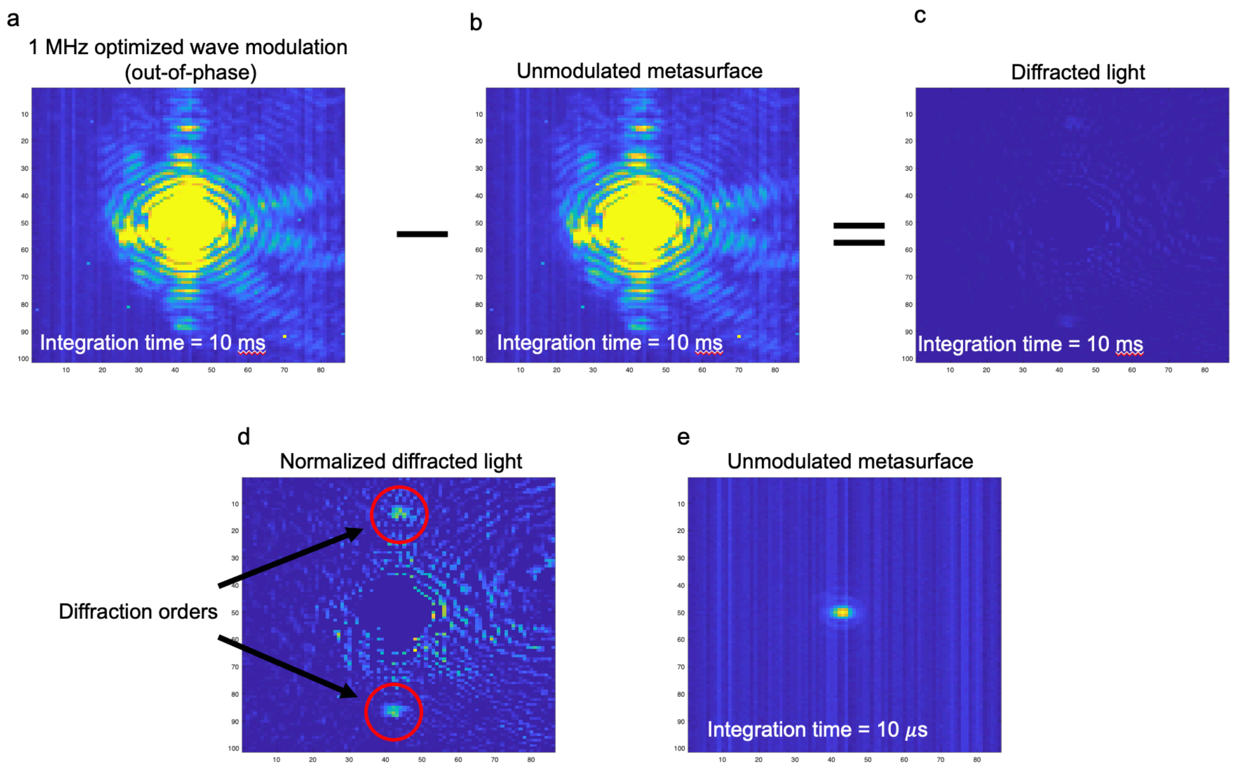

<u>Figure S3:</u> Total efficiency of space-time diffraction. Note: All sub-figures are images taken with a conventional camera placed in the Fourier plane of our imaging setup. (a) Saturated camera image of light reflected from metasurface while modulating with the optimized voltage waveform shown in Fig. 3c from the main text. The waveform is offset by half a period between each metasurface electrode, thus recreating the case shown in Fig. 4b from the main text. (b) Saturated camera image of light reflected from metasurface with equal voltage applied across the metasurface and no temporal modulation. (c) Pixel-by-pixel subtraction of (b) from (a). (d) Data from (c), normalized by the maximum intensity in (c). (e) Camera image of light reflected from metasurface without any modulation, with exposure time decreased to prevent saturation. This is (b) with 1000x smaller integration time.

Our current device displays > 200° phase shift at 1470 nm, compared to the < 20° phase shift at 1530 nm, the operation wavelength used in this work. One could increase the frequency conversion efficiency at each harmonic by operating at 1470 nm. However, due to instrumentation limitations, we were unable to access the wavelength of maximum phase shift using our erbium-doped fiber amplifier (which is limited to operation in the c-band) in our space-time modulation measurements. Further calculations are shown below to illustrate the improvements in efficiency that could be enabled by making use of the greater phase shift at 1470 nm.

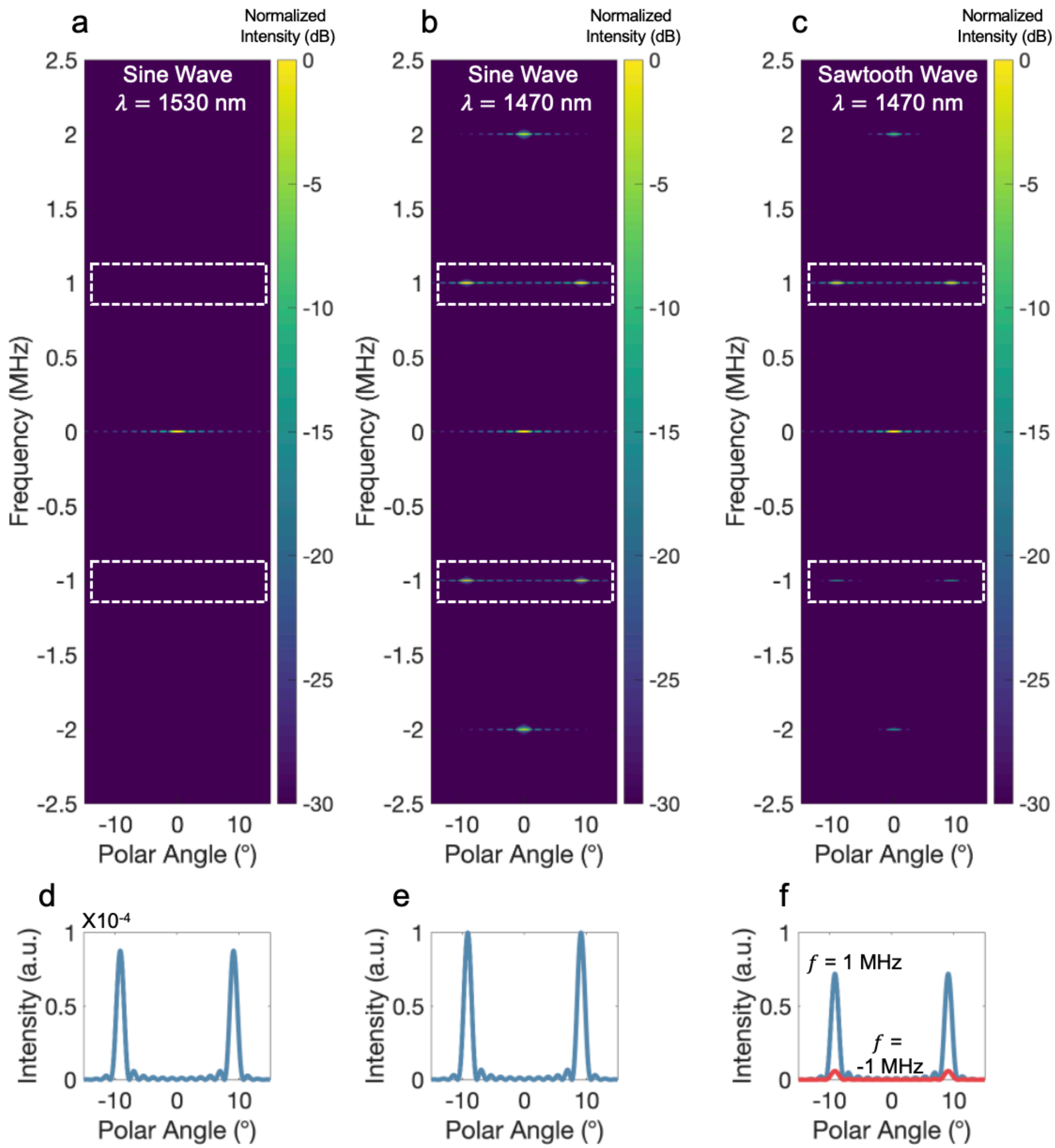

Figure S4: Effect of phase shift on spatiotemporal diffraction efficiency. (a) Calculated far-field intensity when modulating our device at 1530 nm with two 12 V_{p-p} sine waves, offset by half a period. (b)-(c) Calculated far-field intensity when modulating our current device at 1470 nm with two 12 V_{p-p} sine (b) and sawtooth (c) waveforms, offset by half a period. (a)-(c) are plotted in log scale with identical bounds, normalized to the maximum intensity across all angles and frequencies. (d)-(f) Linear spatial cross-sections taken at $f = \pm 1$ MHz, as shown by dotted white boxes in (a)-(c). The amplitude and phase values as a function of voltage at each operating wavelength were taken from measured values. Because of the increased phase shift at 1470 nm, the intensity of light at non-zero frequency shifts is much larger compared to the 1530 nm case, where phase shift is limited. In (d) and (e), the intensity curves are identical at $f = \pm 1$ MHz while the intensity is greater for $f = 1$ MHz in (f) due to the asymmetric sawtooth voltage profile.

As shown in Fig. S4, by operating our devices at a wavelength of 1470 nm, higher conversion efficiency to the generated harmonics is enabled. Figs. S4a-b use identical time-varying driving voltage waveforms, but the available phase shift at 1470 nm results in a larger ratio of modulated to unmodulated light. Additionally, the greater phase shift enables the generation of only positive frequencies when applying an asymmetric waveform (Fig. S4c). By summing the intensities in the diffracted orders at +/- 1 MHz, dividing by the total intensity at all angles and frequencies, and multiplying by the average reflectance, we can obtain the total space-time diffraction efficiencies for each case illustrated above. Note: The average reflectance at 1530 nm is ~23.5% whereas it is ~5% at 1470 nm. The calculated diffraction efficiencies were 0.0076% for sine wave modulation at 1530 nm with only amplitude modulation, 1.86% for sine wave modulation at 1470 nm with > 200° phase shift, and 1.53% for sawtooth modulation at 1470 nm with > 200° phase shift. Thus, by operating our current devices at a wavelength with greater phase shift, one would be able to increase the spatiotemporal diffraction efficiency by a factor of ~245.

The active metasurface community continues to develop devices with higher efficiency, larger phase shift, fast response time, and high spatial resolution of tunability. Improvements in all these of parameters will be key enablers for more efficient space-time modulation.

Regarding the transparent conducting oxide (TCO)-based plasmonic platform that we use in this work: TCO metasurfaces provide many benefits such as large phase shift, ease of electrical modulation with high spatial resolution, and fast modulation speed. However, high absorption losses in the gold and ITO makes it a poor candidate for achieving high efficiency in the long run [6]. Lately, research efforts across the active metasurface community have focused on exploring alternative active modulation schemes using lower loss materials for active permittivity modulation such as phase-change materials, electro-optic materials, and liquid crystals. We will discuss the latest advances for each technology and the limiting factors that currently prevent them from demonstrating efficient space-time modulation in the near-IR. While improvements can be made by utilizing greater phase shift, we are still fundamentally limited by the low reflectance of plasmonic metasurfaces. To improve the total reflectance or transmittance of space-time modulation, novel active metasurface designs are required.

<u>Phase change materials:</u> Active metasurfaces using phase-change materials make use of a large change in the real and imaginary part of refractive index when the material amorphizes or crystallizes into a different phase. While this can provide large optical modulation, the materials require quick heating and cooling to achieve their phase transition which is commonly achieved through Joule heating or pumping with high power lasers. While it is possible to modulate these materials with fs pulsed lasers [7], electrical modulation of phase change material metasurfaces has been limited to 10s of kHz frequencies [8,9]. For use in space-time metasurfaces, modulation frequencies should exceed the linewidth of the incident laser (typically 10s to 100s of kHz). Additionally, due to thermal crosstalk, it can be difficult to achieve the spatial resolution required for a switchable diffraction functionality [10]. With further thermal engineering, these devices may be a suitable platform for space-time modulation, but they are currently limited by slow response time and crosstalk between neighboring elements.

<u>Electro-optic materials:</u> Electro-optic materials offer a promising future for active metasurfaces due to their low loss and fast speeds of electrical modulation [11]. In recent years,

lithium niobate (LN) has emerged as a leading electro-optic material in the photonics community and thin film LN has become commercially available, greatly increasing the accessibility of LN-based devices. Organic electro-optic chromophores have also recently been used to demonstrate GHz amplitude modulation [11]. However, to date, electro-optic designs exhibiting tunable phase shift at subwavelength resolutions while maintaining high optical efficiencies have been shown in theory, but have not been realized experimentally [12,13]. Klopfer *et al.* demonstrated a theoretical metasurface design using high Q-factor resonances with LN to achieve > 80% diffraction efficiency in simulation [12]. By using the simulated phase and amplitude values provided in this work, we calculated a total space-time diffraction efficiency of ~92% by modulating with two waveforms with an amplitude of $\pm$10 V inverse-designed to provide a linearly phase gradient in time. This illustrates that our method presented can be used to obtain high efficiency frequency conversion if a suitable device is available. Thus, electro-optic materials are a promising platform, but tunable phase shift and beam steering have yet to be experimentally realized.

Liquid crystals: Another technique that has shown promise for high efficiency active metasurfaces is the actuation of liquid crystals (LCs), coupled to nano-resonators. While these devices have shown ~360° phase shift while maintaining > 80% reflectance in simulation [14], modulation speeds have been limited to a few kHz due to the slow relaxation time of LCs [14,15]. While techniques are being explored to increase the speed of modulation such as thinning the LC layer and removing alignment layers [16], there is no clear pathway to achieving significantly faster modulation frequencies beyond 10s of kHz.

While there are many exciting emerging technologies that offer the potential to enable active metasurfaces with large phase modulation, high spatial resolution, fast modulation, and high efficiency, this is still an active field of research and we believe that ITO-based plasmonic metasurfaces are an ideal testbed to explore dynamic wavefront shaping at a deeply subwavelength scale, despite their low reflectivity.

S4: Active metasurface phase measurements

Figure S2 plots the maximum phase shift achieved by our active metasurface as a function of wavelength. The largest phase shift occurs between 1465 nm and 1470 nm, corresponding to the minimum reflectance measured in Fig. 2e of the main text. The phase shift of this device at the design wavelength for this work (1530 nm) is near-zero (< 20°). While there is larger amplitude and phase modulation at shorter wavelengths (~1470 nm), we chose to work at 1530 nm because it is the shortest wavelength we could access with sufficient power in our experimental setup. This work could be repeated closer to resonance using the same principles discussed here and the final results would be identical, but the overall efficiency of the device would be higher. Specifically, there would be a higher ratio of total modulated light to unmodulated light (see Supplementary Section 4). However, since our measurement technique already filters out unmodulated light, in this work we are still able to show the same principles of space-time modulation and engineer the power sent to each modulated frequency with good signal-to-noise ratio (SNR).

It is noteworthy that this work demonstrates space-time diffraction with excellent directivity at each modulated frequency using a device with such limited reflectance and phase modulation. If this device was modulated in the quasi-static regime, it would exhibit very low diffraction efficiency (see Supplementary Section 9). By using space-time modulation, roughly the same total amount of light is diffracted as in the quasi-static case, but the light sent to the +/- 1st orders are separated in frequency from the 0th order (normally reflected light) which allows for easier detection with high SNR. This is a major benefit of space-time metasurfaces.

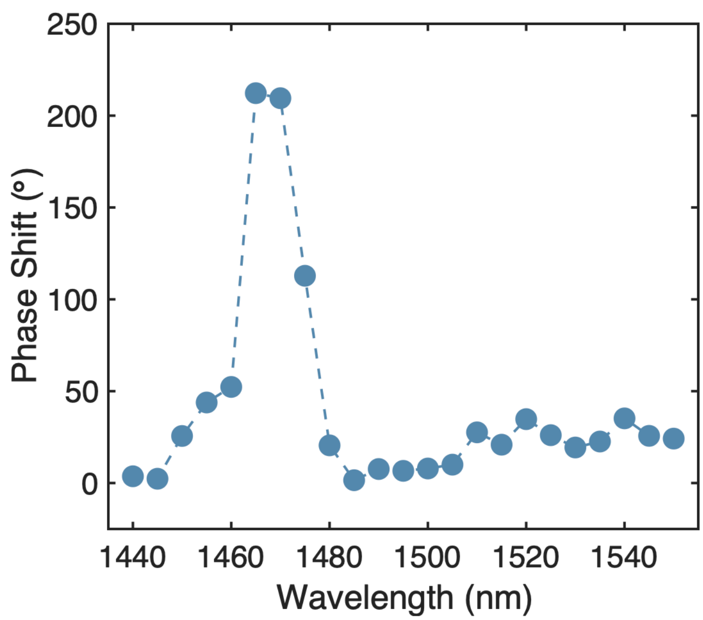

Figure S2: Quasi-static phase shift of the active metasurface used in this work. The plotted phase shift is the absolute value of the change in phase between an applied bias of -6 V and 6 V.

S5: Frequency-response of ITO-based metasurfaces

In this work, the frequency of modulation is limited by the detection scheme, not the metasurface device. The 3 dB cutoff of the photodiode used is 10 MHz (ThorLabs APD410C) and we chose to modulate at 1 MHz to ensure that we can sufficiently resolve higher order harmonics without losing collected signal. Since the carrier modulation in ITO occurs in a small layer (< 17 nm) the carrier accumulation occurs very quickly. Previous demonstrations have experimentally demonstrated ITO modulators reaching GHz speeds [17,18]. Because of this, we do not expect the ITO response time to be a limiting factor at MHz frequencies. A more probable limitation could come from the RC time constant of our driving circuits.

To estimate the frequency response of the interconnects and antennas driving our metasurface, we used a simple RC time-constant estimate based on the geometry of our device. By doing this, we calculate, for one metasurface antenna group (consisting of 156 individual nanoantennas), a resistance of ~ 2 Ω and a capacitance of ~ 50 pF resulting in a RC-limited frequency of ~ 1.6 GHz. A plot of the characteristic frequency of the antenna groups as a function of antenna length is plotted in Fig. S5a. The antennas for the metasurfaces in this work are 120 μm long. Next, we examined the frequency response of the fabricated interconnects that electrically address each antenna group. These interconnects are of varying length (~50 μm to 1mm) and width (~2.5 μm to 20 μm). Figure S5b plots the characteristic frequency for these interconnects of varying length and width, by calculating the resistance and self-inductance of the lines. Using these estimates, Fig. S5 shows that for all considered dimensions of nanoantennas and interconnects, the characteristic frequency remains above 100 MHz. Therefore, the electrical connections in our device will not limit modulation at 1 MHz.

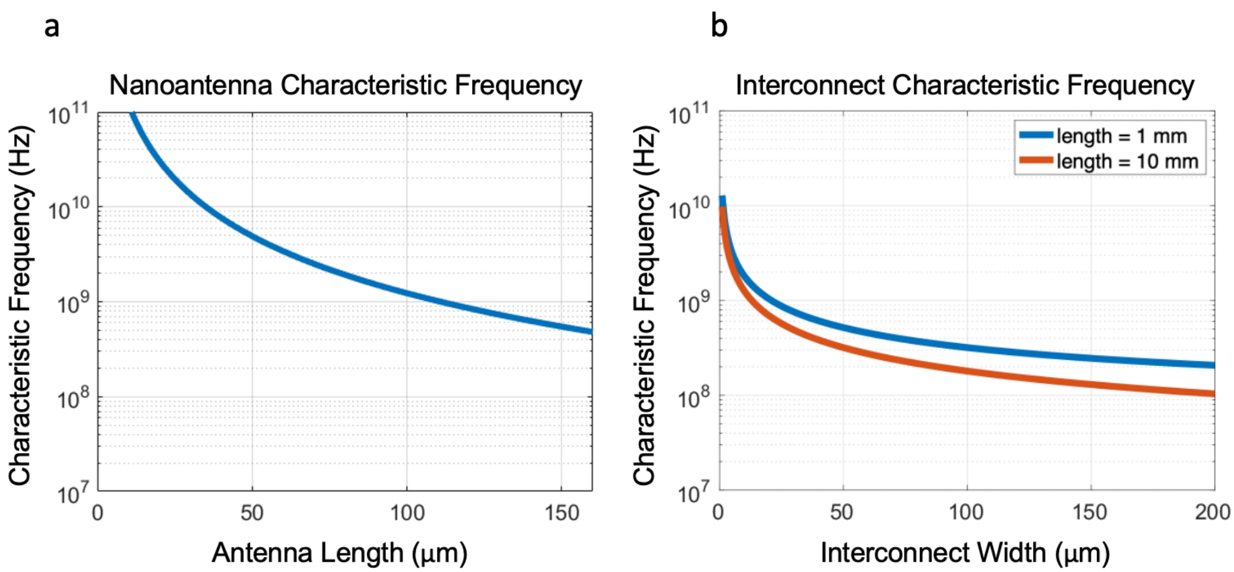

Figure S5: Frequency response of metasurface. (a) Characteristic frequency of metasurface nanoantennas as a function of antenna length. (b) Characteristic frequency of interconnects of varying length as a function of interconnect width.

S6: Waveform optimization algorithm

For our experimental waveform optimizations, we used the open-source genetic algorithm library in python, PyGAD. Each optimization starts by modeling the driving voltage waveform as a 20-term Fourier series with 1 MHz as the fundamental harmonic. The amplitude and phase of each harmonic term are used as inputs (or genes) to be fitted by the genetic algorithm, using random values between -1 and 1 as initial values. For each algorithm iteration, a new driving waveform was sent to the metasurface, and the reflected frequency spectrum was saved. The power at each integer harmonic frequency of 1 MHz up to 10 MHz was saved to be used for calculation of the figure-of-merit (FOM), which was maximized by the genetic algorithm over multiple generations. The genetic algorithm optimization parameters used were:

Number of generations = 80
Number of parents mating = 8
Solutions per population = 40
Number of genes = 40
Initial range low = -1
Initial range high = 1
Parent selection type = rank
Number of parents to keep = 4
Random mutation minimum value = -1
Random mutation maximum value = 1
Crossover type = single point
Mutation type = random
Mutation percent genes = 20
Elitism = 2

These genetic algorithm parameters were kept constant for all optimizations, and the FOM was changed in order to obtain each frequency spectrum of interest. The FOMs used for each frequency spectrum shown in the main text are shown in Table S1.

Note: The variable, 'power', will be used in the FOM definitions below. This is a 1D array of the measured powers at integer frequencies from 1 to 10 MHz. The indexing and manipulation of this array will follow the convention used in python. Example #1: power[0] = measured power at 1 MHz, Example #2: sum(power[2:])= the sum of all powers measured at integer frequencies from 3 MHz to 10 MHz.

Table S1: Genetic algorithm figures-of-merit

Frequency spectrum	FOM definition
Maximize 1^{st} harmonic while suppressing all others (Fig. 3 and 4 of main text)	$FOM1 = \frac{power[0]}{sum(power[1:])}$
Maximize 3^{rd} and 5^{th} harmonic with equal intensities while	$rel = \frac{power[2] * power[4]}{power[0] + power[1] + power[3] + sum(power[5:])}$

suppressing all others (Fig. 5a-c of main text)	$$av = \frac{power[2] + power[4]}{2}$$ $$FOM2 = rel - abs(power[2] - av) - abs(power[4] - av)$$
Maximize 1st through 5th harmonics while suppressing all others (Fig. 5d-I of main text)	$t1 = power[0]\ from\ optimized\ wave\ using\ FOM1$ Note: This is the power measured at 1 MHz when modulating metasurface with the final optimized wave produced using FOM1. It is used as a target power for the first 5 harmonics here. $t2 = power[2]\ from\ optimized\ wave\ using\ FOM2$ Note: This is the power measured at 3 MHz when modulating metasurface with the final optimized wave produced using FOM1. It is the floor of our measurement and is used as a target power for the last 5 harmonics here. $$dev1 = \sum_{i=0}^{4} abs\left(log_{10}\left(abs(\,power[i] - t1)\right)\right)$$ $$dev2 = \sum_{i=5}^{9} abs\left(log_{10}\left(abs(\,power[i] - t2)\right)\right)$$ $$FOM = \frac{1}{dev1 + dev2}$$

It should be noted that the selected FOMs are not necessarily the most efficient definitions to achieve the presented frequency spectra. They provided the desired frequency response in a reasonable number of algorithm iterations and are presented here for the reader's interest.

S7: Modulation of the average reflectance/varying reflectance between two electrodes

Throughout our space-time modulation measurements in the main text, we repeatably have signal at 0° (0^{th} spatial order) at each diffracted frequency. In most cases, the power sent to the 0^{th} order is much less than the +/- 1^{st} orders at a given frequency, but in this section, we investigate the cause of this unwanted signal.

Any modulated intensity at the 0^{th} spatial order is a result of the total reflectance from the metasurface (i.e., average reflectance across the entire metasurface area) changing in time. Because the optimized waveforms applied to our metasurface are not symmetric about a given voltage, we would expect the time-dependent reflected field profile to also not be symmetric. If this is the case, when we time-delay a waveform, we expect the average of the reflectance for each waveform to change in time and produce a modulated signal at the 0^{th} spatial order. Figure S6 below explores this further.

Figure S6a plots the time-varying reflectance for each metasurface electrode when the metasurface is driven in the configuration shown in Fig. 4b from the main text. The average reflectance at each point in time, using the data from Fig S6a, is plotted in Fig. S6b and confirms that the average reflectance is in fact changing in time. Figure S6c plots the magnitude squared of the Fourier transform of the average time-varying amplitude (square root of the signal in Fig. S6b) to show the expected frequency spectrum at the 0^{th} spatial order in this driving scheme. Comparing this result to the measured data from Fig. 4c in the main text, the signal at 2 MHz is present, but the measured 1 MHz signal at the 0^{th} spatial order is still not accounted for.

In order to explain the 1 MHz signal at the 0^{th} spatial order, we hypothesized that this was caused by a slightly different reflectance response between the two electrodes of our metasurface. This could be caused by an inhomogeneous distribution of trapped charges in our dielectric, resulting in different band offsets between each electrode group. If this was the case, the average metasurface reflectance would be different than Fig. S6b and may contain a non-zero 1 MHz signal. To verify this idea, we assumed that one electrode had its reflectance modulation depth decreased by 10%. This case is shown in Fig. S6d where we again assume the same driving waveform as Fig. S6a but decreased the modulation depth of electrode 1 by 10%. Figure S6e plots the average reflectance from the metasurface and Fig. S6f plots the expected frequency response at the 0^{th} spatial order (magnitude squared of the Fourier transform of the square root of Fig. S6e). As expected, when the two electrodes of the metasurface do not modulate exactly the same, we see some 1 MHz signal at the 0^{th} spatial order. Unlike our measurement, the power at 1 MHz in Fig. S6f is less than the power at 2 MHz. However, the assumed 10% decrease in reflectance modulation is fairly small and if the difference in the response of the electrodes is larger in experiment, we would expect to see a much larger signal at 1 MHz in the 0^{th} spatial order.

If one wanted to decrease the 0^{th} spatial order signal at modulated frequencies, the optimization algorithm used to obtain the time-varying waveform could be generalized to optimize for the driving waveform for each electrode independently. By doing this, we could account for any difference in response between the two metasurface electrodes. However, for this demonstration, we were still able to demonstrate good directivity of diffraction at each frequency of interest and did not believe that this optimization was within the scope of this work.

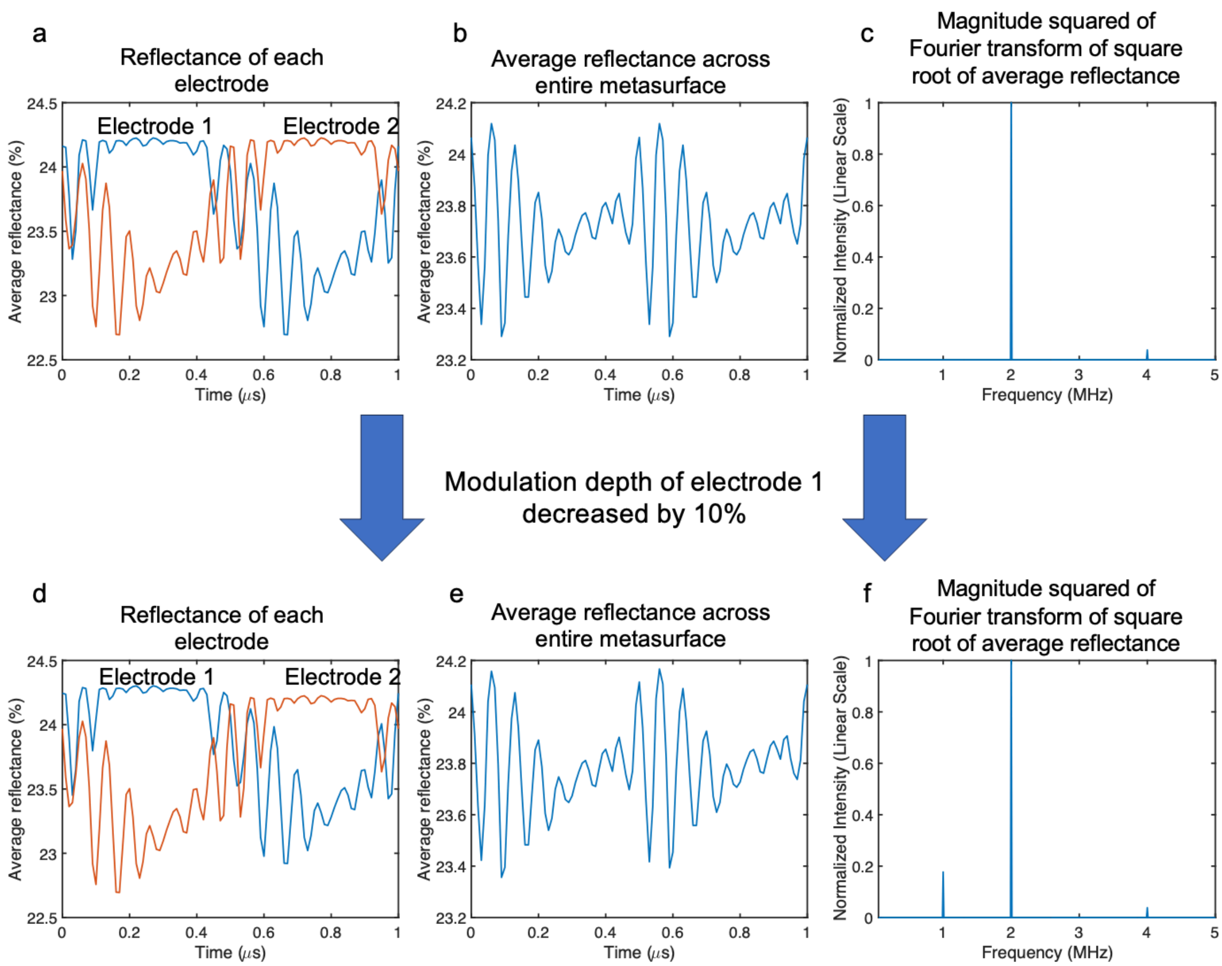

Figure S6: Investigation of average reflectance modulation from metasurface. For all data presented here, the optimized waveform shown in Fig. 3c in the main text is used, offset by half a period between each electrode. (a) Reflectance of each electrode across the metasurface over one period. (b) Average reflectance of each electrode from (a) at each point in time. (c) Magnitude squared of one-sided Fourier transform of square root of (b). (d) Reflectance of each electrode across the metasurface. The modulation depth of electrode 1 is decreased by 10%. (e) Average reflectance of each electrode from (d) at each point in time. (f) Magnitude squared of one-sided Fourier transform of square root of (e).

S8: Experimental setup for space-time measurements

Figure S7 shows a schematic of the experimental setup used to obtain the measurements of reflected intensity as a function of frequency and angle presented in Figs. 4 and 5 of the main text. Laser light with a wavelength of 1530 nm is emitted from a continuous-wave laser and sent through a polarizer and half-waveplate to control the polarization to be orthogonal to the antennas on the metasurface. Next, an iris decreases the beam size of the laser and it is focused by a 300 mm lens to the back focal plane of a 20x infinity-corrected near-infrared (IR) objective which roughly collimates the laser light on the metasurface. The metasurface is modulated at 1 MHz with an arbitrary wave and the reflected light from the metasurface is collected again by the near-IR objective and 300 mm lens before the light is reflected away from the laser using a beam splitter. Finally, a 200 mm lens is used to focus the light, and a photodiode (connected to a spectrum analyzer) is placed in the Fourier plane after this lens. The photodiode is mounted on a two-axis motorized stage and is scanned in the XY plane (each point corresponds to a different angle of light reflected from the metasurface). At each point in the XY plane, three frequency spectra are collected and averaged. Since the metasurface only diffracts light in one dimension, we would ideally only need to scan the photodiode in one axis, assuming everything is perfectly aligned. However, there is inevitably some misalignment between the direction of diffraction from our metasurface and the scan direction of our photodiode. Thus, we scan the photodiode across a two-dimensional space in the Fourier plane and then extract a line cut that connects the maxima of the two diffracted orders and the 0^{th} order. Using this experimental setup, we collect intensity as a function of frequency and position in the Fourier plane which allows us to generate the intensity versus frequency and angle plots presented in Figs. 4 and 5 of the main text.

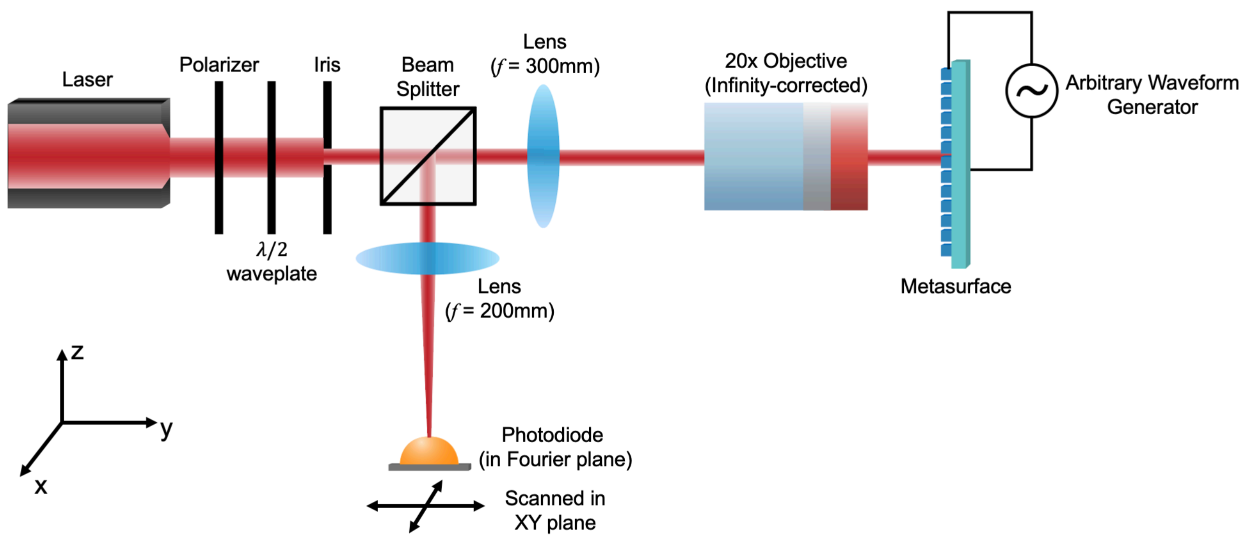

Figure S7: Optical setup used for space-time measurements. The metasurface is illuminated with linearly polarized laser light, modulated with an arbitrary waveform at 1 MHz, and the reflected light from the metasurface is measured by a photodiode placed in the Fourier plane, connected to a spectrum analyzer.

It should be noted that since the active area of our metasurfaces is ~ 120x120 μm^2, the 20x objective is needed to first image the metasurface and ensure it is being fully illuminated by the laser. In practice, the optical setup in Fig. S7 is first used by removing the 200 mm lens and replacing the photodiode with an IR camera. By doing this, we are able to image the metasurface area with enough magnification to align the beam properly and close the iris to ensure that only the active area of the metasurface is illuminated. Once everything is set up properly, we insert the 200 mm lens to image the Fourier plane and replace the camera with the photodiode. By keeping the 200 mm lens after the beam splitter, we ensure that the metasurface illumination remains the same. Multiple x-y scans of the photodiode are also performed at various z-axis positions before a final scan is performed to ensure that the photodiode is placed perfectly in the Fourier plane.

S9: Quasi-static performance of active metasurface

It is useful to compare the total diffraction efficiency of our metasurface during space-time modulation to the maximum achievable diffraction efficiency in the quasi-static regime. Supplementary Section 4 already discussed the measured and calculated diffraction efficiency of our space-time metasurface. For simplicity, we used the following definition of diffraction efficiency:

$$\eta = \frac{P_{-1} + P_{+1}}{P_{-1} + P_{+1} + P_0} \times \bar{R} \qquad (1)$$

where $P_{-1,0,+1}$ refer to the power (integrated intensity) in the -1st, 0th and +1st diffraction orders, respectively, and $\bar{R}$ is the average total reflectance. In the space-time modulated case, the measured and calculated diffraction efficiencies were 0.0036% and 0.0017%, respectively (see Supplementary Section S3).

In the case of quasi-static diffraction, we will assume that one electrode is held at -4 V and the other at +4 V to achieve the maximum reflectance contrast possible of 22.6% and 24.2% (see Fig. 2f from the main text). Using these reflectance values, we performed a discrete array factor calculation to calculate the far-field intensity under this condition (Fig. S8). Using the definition provided in Equation 1, we obtained a total efficiency of 0.14%. As expected, this efficiency is larger (~39 times) than the measured spatiotemporal diffraction efficiency. This is because during quasi-static operation, the metasurface is fixed at the largest possible amplitude contrast between the two electrodes. However, during space-time modulation, the amplitude changes over time and there will always be equal or less contrast at any given point in time than the quasi-static case, resulting in less diffracted power when integrated over time.

While space-time modulation did not improve the total diffraction efficiency compared to the quasi-static case, its ability to separate the diffracted light in frequency from 'non-diffracted' light greatly improves the SNR of diffraction at the frequency of interest. This could be useful in applications if one can install bandpass filters on the detectors of interest to only select for the desired generated frequencies.

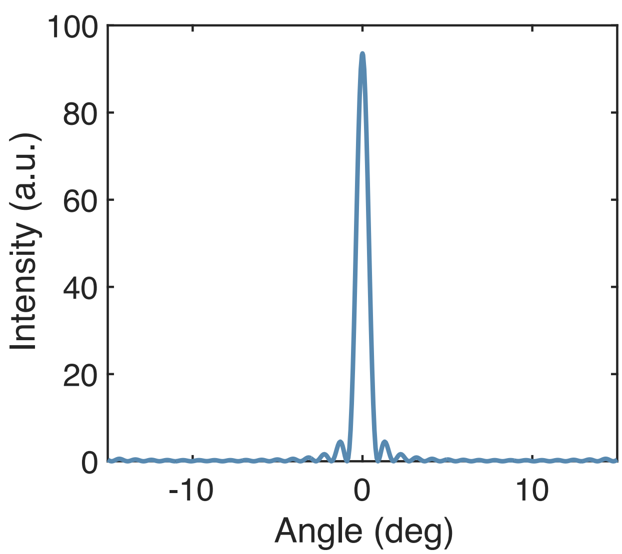

Figure S8: Calculated field profile during quasi-static diffraction.

Supplementary References

1. Song, X. *et al.* Switchable metasurface for nearly perfect reflection, transmission, and absorption using PIN diodes. *Opt Express* **29**, 29320 (2021).
2. Zhang, L. *et al.* Space-time-coding digital metasurfaces. *Nat Commun* **9**, (2018).
3. Ahadi, S., Neshat, M. & Moravvej-Farshi, M. K. Binary THz modulator based on silicon Schottky-metasurface. *Sci Rep* **12**, 18871 (2022).
4. Huang, C. *et al.* Dynamical beam manipulation based on 2-bit digitally-controlled coding metasurface. *Sci Rep* **7**, 42302 (2017).
5. Thureja, P. *et al.* Array-Level Inverse Design of Beam Steering Active Metasurfaces. *ACS Nano* **14**, 15042–15055 (2020).
6. Sokhoyan, R. *et al.* Electrically tunable conducting oxide metasurfaces for high power applications. *Nanophotonics* **12**, 239–253 (2023).
7. Michel, A.-K. U. *et al.* Reversible Optical Switching of Infrared Antenna Resonances with Ultrathin Phase-Change Layers Using Femtosecond Laser Pulses. *ACS Photonics* **1**, 833–839 (2014).
8. Abdollahramezani, S. *et al.* Electrically driven reprogrammable phase-change metasurface reaching 80% efficiency. *Nat Commun* **13**, 1696 (2022).
9. Wang, Y. *et al.* Electrical tuning of phase-change antennas and metasurfaces. *Nat Nanotechnol* **16**, 667–672 (2021).
10. Zhang, Y. *et al.* Electrically reconfigurable non-volatile metasurface using low-loss optical phase-change material. *Nat Nanotechnol* **16**, 661–666 (2021).
11. Benea-Chelmus, I. C. *et al.* Gigahertz free-space electro-optic modulators based on Mie resonances. *Nat Commun* **13**, (2022).
12. Klopfer, E., Dagli, S., Barton, D., Lawrence, M. & Dionne, J. A. High-Quality-Factor Silicon-on-Lithium Niobate Metasurfaces for Electro-optically Reconfigurable Wavefront Shaping. *Nano Lett* **22**, 1703–1709 (2022).
13. Weiss, A. *et al.* Tunable Metasurface Using Thin-Film Lithium Niobate in the Telecom Regime. *ACS Photonics* **9**, 605–612 (2022).
14. Moitra, P. *et al.* Electrically Tunable Reflective Metasurfaces with Continuous and Full-Phase Modulation for High-Efficiency Wavefront Control at Visible Frequencies. *ACS Nano* **17**, 16952–16959 (2023).
15. Abu Aisheh, M., Abutoama, M., Abuleil, M. J. & Abdulhalim, I. Fast tunable metamaterial liquid crystal achromatic waveplate. *Nanophotonics* **12**, 1115–1127 (2023).
16. Maruthiyodan Veetil, R. *et al.* Nanoantenna induced liquid crystal alignment for high performance tunable metasurface. *Nanophotonics* **0**, (2023).
17. Gui, Y. *et al.* 100 GHz micrometer-compact broadband monolithic ITO Mach–Zehnder interferometer modulator enabling 3500 times higher packing density. *Nanophotonics* **11**, 4001–4009 (2022).
18. Amin, R. *et al.* Sub-wavelength GHz-fast broadband ITO Mach–Zehnder modulator on silicon photonics. *Optica* **7**, 333 (2020).